Control of optical contrast using gold nanoshells for optical coherence tomography imaging of mouse xenograft tumor model *in vivo*

James Chen Yong Kah
National University of Singapore
Division of Bioengineering
7 Engineering Drive 1
Blk E3A, #04-15
Singapore, 117574

Malini Olivo
National Cancer Center Singapore
Division of Medical Sciences
11 Hospital Drive
Singapore 169610
    and
Singapore Bioimaging Consortium
Biomedical Sciences Institutes
11 Biopolis Way
#02-02 Helios
Singapore, 138667
    and
National University of Singapore
Department of Pharmacy
18 Science Drive 4
Singapore, 117543

Tzu Hao Chow
Kin San Song
Nanyang Technological University
School of Electrical and Electronics Engineering
50 Nanyang Avenue
Singapore, 639798

Karen Zhen Yu Koh
Subodh Mhaisalkar
Nanyang Technological University
School of Materials Science and Engineering
Block N4.1 Nanyang Avenue
Singapore, 639798

Colin James Richard Sheppard
National University of Singapore
Division of Bioengineering
Block E3A #04-15
7 Engineering Drive 1
Singapore, 117576
E-mail: colin@nus.edu.sg

Abstract. The control of image contrast is essential toward optimizing a contrast enhancement procedure in optical coherence tomography (OCT). In this study, the *in vivo* control of optical contrast in a mouse tumor model with gold nanoshells as a contrast agent is examined. Gold nanoshells are administered into mice, with the injected dosage and particle surface parameters varied and its concentration in the tumor under each condition is determined using a noninvasive theoretical OCT modeling technique. The results show that too high a concentration of gold nanoshells in the tumor only enhances the OCT signal near the tissue surface, while significantly attenuating the signal deeper into the tissue. With an appropriate dosage, IV delivery of gold nanoshells allows a moderate concentration of 6.2×10^9 particles/ml in tumor to achieve a good OCT signal enhancement with minimal signal attenuation with depth. An increase in the IV dosage of gold nanoshells reveals a corresponding nonlinear increase in their tumor concentration, as well as a nonlinear reduction in the fractional concentration of injected gold nanoshells. Furthermore, this fractional concentration is improved with the use of anti-epodermal growth factor receptor (EGFR) surface functionalization, which also reduces the time required for tumor delivery from 6 to 2 h.
© 2009 Society of Photo-Optical Instrumentation Engineers. [DOI: 10.1117/1.3233946]

1 Introduction

In biomedical imaging of tissues, it is often desirable to enhance the signal measured from specific structures. For most imaging modalities, the effectiveness of medical images has been enhanced with the aid of contrast agents. These agents that selectively localize at specific organ sites or tissues of interest to produce specific image signatures have been successfully utilized in almost every medical imaging technique, including ultrasound, computed tomography (CT), magnetic resonance imaging (MRI), and optical microscopy.

Optical coherence tomography (OCT) is an emerging biomedical imaging modality that shows promise for a wide range of biomedical applications.[1] It is a noninvasive method for cross sectional subsurface imaging of tissue up to a depth of 2 mm with a high spatial resolution of 10 to 15 μm, based

Address all correspondence to: Colin James Richard Sheppard, Professor, Division of Bioengineering, National University of Singapore, Block E3A, #04-15, 7 Engineering Drive 1, Singapore 117576. Tel: 65 65161910; E-mail: colin@nus.edu.sg

on interference detection of optical echoes of light backscattered in the near-infrared (NIR) region (0.75 to 1.3 μm). This region is of biological significance, as it provides a window in the spectrum where the components of tissue do not have significant absorption,[2] thus promoting maximum light penetration for imaging. The principles of OCT have been previously described.[1,3] OCT is already used as a standard imaging modality in ophthalmology to visualize retinal anatomy,[4] and its potential in gastroenterology,[5–8] gynecology,[9] and cardiology[10,11] is under investigation. Since OCT is capable of cellular-resolution imaging, it has proved to be an efficient technique for *in vivo* imaging of superficial tissues such as skin and mucous membranes,[10,12] and may ultimately have a role in the diagnosis of early human malignancies[9,13–15] as well as identifying tumor margins in real time without the need for tissue biopsy.[16]

The source of contrast in OCT is a change in the index of refraction. In turbid tissues, there are many microscopic refractive index mismatches within a resolution element of the OCT system. Thus, the OCT signal received is a general measure of the backscattering properties of the tissue. Tissue layers can often be distinguished by a difference in their backscattering properties compared to adjacent layers. In general, while OCT images have proven to be very useful in identifying normal and pathological tissues such as actinic keratosis,[17] colon adenomas and carcinomas,[18,19] and developing cardiac tissue,[20] imaging in OCT is frequently hindered by poor contrast between adjacent tissues. Although morphological differences between normal and neoplastic tissues can be obvious at later stages of tumor development, it is challenging to detect early stage tumors that are morphologically (or optically) similar to surrounding normal tissues.

Contrast agents are often used to increase the diagnostic and analytical capabilities of imaging modalities by site-specific labeling of tissues of interest. By targeting contrast agents to a tissue of interest, their image can be improved to highlight the tissue and provide a clear demarcation between the selected tissue and their surroundings. Therefore, a selective optical agent for contrast enhancement on a specific site of interest would be useful to better differentiate tissue types with similar scattering properties, detect subtle changes in tissue morphology, and identify early cancerous changes in human tissues that are morphologically similar to surrounding normal tissues. This holds true for OCT imaging, where the use of contrast agents offers the promise of enhanced diagnostic power with the potential to overcome the limitation of relying on inherent optical properties to discriminate pathology. Since OCT detects scattering changes, image contrast enhancement can be achieved by delivery of highly scattering contrast agents into the tissue, allowing them to localize to specific regions of interest. Thus, tissues with injected contrast agents would scatter more light back from regions of interest to produce a stronger OCT signal, which is detected to form a contrast-enhanced OCT image.

The traditional way of improving image contrast in OCT images employs the use of osmotically active immersion liquids such as glycerol, propylene glycol, dextranes, and concentrated glucose solution.[21,22] Other types of contrast agents with particulate natures, such as air-filled microbubbles[23,24] and engineered microspheres with a protein shell,[25] have also been designed to increase the backscattered light intensity and alter the local optical properties of tissue to enhance the utility of OCT. Despite promising results with ≈5% improvement in optical contrast obtained with microbubbles,[26] particulate contrast agents for OCT can be improved to further enhance image contrast *in vivo* by introducing smaller nanometer alternatives to engineered microspheres (≈2 to 15 μm) to improve their distribution in microcirculation.

In the present work, we present an approach to OCT imaging using gold nanoshells as a contrast agent. Being effective for backscattering types of imaging *in vitro*,[27,28] gold nanoshells could can also be a potentially effective contrasting agent for OCT. The effectiveness of using gold nanoshells in enhanced OCT imaging has been demonstrated.[26,27,29] Gold nanoshells possess a core-shell structure comprised of a metallic gold layer surrounding a dielectric core such as silica, that is capable of exhibiting a strong optical extinction at visible and NIR wavelengths to produce enhanced optical backscatter. This is due to a localized surface plasmon resonance of their free electrons on excitation by an electromagnetic field.[30] Because OCT detects light backscattered at index of refraction mismatches in tissues, it is anticipated that the gold nanoshells with very high scattering efficiency and minimal absorption at the OCT NIR source wavelength would therefore produce a strong OCT signal that is detectable in the midst of highly scattering tissue.[27,29] This optical resonance can be custom-tuned anywhere in the spectrum from the visible through the NIR by varying the relative size of the core and the thickness of the shell[31] for compatibility with the specific imaging source wavelength. Gold nanoshells are also small (<300 nm) and biologically inert,[32] thus making them suitable for *in vivo* use.

O'Neal et al.[33] reported on the use of polyethylene glycol-coated gold nanoshells (≈130 m in diameter) that localize in the tumor passively after IV delivery due to the enhanced permeability and retention (EPR) effect, by which nanoscale materials are preferentially deposited in tumors (as opposed to normal tissue), as they passively extravasate through the leaky and aberrant tumor vasculature.[34,35] This passive nanoparticle localization in the tumor can be detected by the optical contrast that the gold nanoshells elicit under OCT. However, gold nanoshells may also be tailored to adhere to specific molecules, cells, or tissue types to provide additional selectivity for imaging. This is effected through appropriate surface functionalization, for example by conjugation with antibody or proteins to facilitate interaction between tumor cell surface receptors and receptor ligands attached to gold nanoshells.

Despite the successful demonstration of gold nanoshells as an OCT contrast agent, there are at least three identified issues that should be addressed for a more effective imaging *in vivo*. First, the available *in vivo* experimental data are insufficient for developing an appropriate contrasting procedure, since detailed parametric studies such as dosage of gold nanoshells administered have not been performed to demonstrate control of optical contrast *in vivo*. Second, while targeting of macromolecular anticancer drugs has been studied in detail, less is known about the dynamics of EPR for metal nanoparticles *in vivo* primarily due to the lack of techniques to monitor them in a tissue noninvasively. For example, the current standard method to measure gold nanoshell concentrations in tissue is neutron activation analysis (NAA),[36] which requires tissue excision, dehydration, and irradiation within a nuclear reactor.

While extremely sensitive, this method is invasive and requires animal sacrifice. Thus, it is not appropriate for longitudinal monitoring of metal nanoparticle distribution in living systems. Third, although improvement in optical contrast of tumor cells has been widely demonstrated *in vitro* using antibody conjugated gold nanoparticles of various shapes, including spherical gold nanoshells,[27] gold nanocages,[37] targeted to HER-2/*neu* receptors, and gold nanorods targeted to epidermal growth factor receptor (EGFR),[38] there is an entire scientific community struggling with the use of such antibody conjugated nanoparticles for *in vivo* targeting, and the amount of published data, while available,[39–42] is lacking.

In this study, we aim to address the issues described by demonstrating the control of optical contrast of tumors grown in a murine *in vivo* model through varying the concentration of injected gold nanoshells and the use of appropriate antibody surface functionalization on gold nanoshell delivery to tumors. Here, the definition of contrast that we adopt is that of the difference in the image signal of the tissue before and after administering the contrast agent. We also develop a noninvasive technique to determine the gold nanoshell concentration in tumor tissue of live mice based on the theoretical modeling of OCT backscattering signal profile.

Our approach involves examining the optical contrast with different modes of nanoshell delivery into tumor tissue, i.e., intratumoral and IV, different concentrations of gold nanoshells injected via IV, and the use of antibody conjugated gold nanoshells compared to nonfunctionalized gold nanoshells, as well as estimating the concentration of gold nanoshells in the tumor tissue under these different delivery regimes. The purpose of introducing the gold nanoshells via intratumoral route is to illustrate the effect of oversaturated scattering on the OCT image with a high concentration of gold nanoshells in the tumor. A covalent antibody conjugation method was previously demonstrated[43] to produce antibody conjugated gold nanoshells with excellent colloidal stability. The selective targeting of epidermal growth factor receptor (EGFR) positive cancer cells *in vitro* using an anti-EGFR monoclonal antibody has also been demonstrated.[44,45] EGFR is a transmembrane glycoprotein that is frequently overexpressed in a variety of solid tumors[46–48] and is used as our cancer marker in this study. The results in this study demonstrate successful control of optical contrast *in vivo*. The *in vivo* estimation of gold nanoshell concentration in tumors is briefly discussed and cross-examined with the optical contrast in imaging to give a better understanding of the dynamics of tumor delivery under different circumstances.

2 Materials and Methods

2.1 Synthesis and Surface Functionalization of Gold Nanoshells

Gold nanoshells were synthesized and pegylated according to our previously published protocol.[49,50] For antibody conjugation, the monoclonal anti-EGFR (Santa Cruz Biotechnology Incorporated, Santa Cruz, California) was conjugated to gold nanoshells using poly(ethylene)glycol SH-PEG-COOH (MW =3000 g/mol, Celares GmbH, Berlin) as the linker with methoxy-poly(ethylene glycol)-thiol (mPEG-thiol) (MW =2000 Da, ≥92%, Celares GmbH) functioning as spacers in between. The mixture of both PEGs containing nine parts of

mPEG-thiol to 1 part SH-PEG-COOH was attached to the gold nanoshells by incubating 1 ml of the described mixture (10 mg/ml) with 1 ml of the gold nanoshells (2.0 $\times 10^{13}$ particles/ml) under water bath sonication for 5 min at room temperature as described. After several washes to remove excess PEGs, the carboxylic end of the linker was then attached to the amine groups on the anti-EGFR via carbodiimide chemistry to form an amide bond. This was done with the aid of 200 μl each of 400-mM 1-ethyl-3-(3-dimethylaminopropyl)-carbo (EDC) (Sigma-Aldrich, Sant Louis, Missouri) and 100 mM of N-hydroxysuccinimide (NHS) (Sigma-Aldrich) as activators added to 1 ml of the pegylated gold nanoshells and incubated for about 20 min at room temperature, before the addition of 20 μl (i.e., 4 μg) of the anti-EGFR. The conjugation was completed within 1 h at room temperature. The pegylated and antibody conjugated gold nanoshells were then rinsed before being redispersed in 2 ml of phosphate buffer solution (1× PBS, pH 7.4) to a final concentration of 2.0×10^{13} particles/ml, as determined by correlating its extinction spectroscopy data to the theoretical extinction cross section data of the gold nanoshells based on the Mie theory. The synthesized gold nanoshells were stored at 4 °C until further use.

The particle size was characterized by transmission electron microscopy (TEM) (Jeol JEM-1010, Jeol, Tokyo) operating at 100 kV. Gold nanoshells with a 162-nm-diam silica core surrounded by a gold shell of 23 nm thickness were synthesized in this process. This size configuration was selected based on an optimized backscattering cross section at 840 nm as predicted from the Mie theory. Their extinction spectrum was measured using a UV-VIS spectrophotometer (Shimadzu UV-2401 PC, Shimadzu, Kyoto, Japan) in the wavelength range from 400 to 900 nm, and compared to the theoretically predicted spectrum determined from a program written in Matlab that calculates the theoretical optical spectra of core-shell structures based on the Mie theory for a single gold nanoshell of the same size configuration.[51]

2.2 Mouse Xenograft Tumor Model

The mouse xenograft tumor model used in this study was developed on male Balb/c nude mice obtained from the Animal Resource Centre (ARC, Western Australia). The mice were 6 to 8 weeks of age and weighed an average of 24 to 25 g. Approximately 5.0×10^6 human epidermoid carcinoma cell line, A-431 (ATCC) suspended in 150 μl of Hanks' balanced salt solution (HBSS) (Gibco, Carlsbad, California) were injected subcutaneously into the lower flanks of the mice to establish the xenograft tumor model. The tumors were allowed to grow to 5 to 6 mm in diameter approximately after 14 days of inoculation before OCT imaging was carried out. All handling procedures for mice were approved by the Institutional Animal Care and Use Committee (IACUC) at SingHealth, Singapore, in accordance with international standards.

2.3 Small Animal Optical Coherence Tomography Imaging

Prior to imaging, the pegylated gold nanoshells were suspended in HBSS to various concentrations and administered into the mice via intratumoral or IV injection. For the intratumoral injection, the mouse was first anaesthetized before
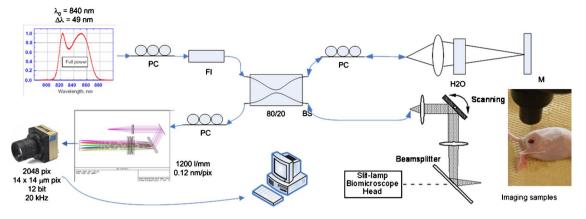
Fig. 1 The schematic of the spectral domain OCT imaging system used in this study. Image courtesy of Bioptigen Incorporated. The setup for imaging various samples such as phantom and small animal models is shown as an inset in the figure.

150 μl of the gold nanoshells (9.0×10^{10} particles/ml) was directly injected with care into the tumor to minimize leakage. For the IV delivery, 150 μl of the pegylated gold nanoshells of four different concentrations: 1.1×10^{10}, 2.3×10^{10}, 4.5×10^{10}, and 9.0×10^{10} particles/ml were injected into the tail vein and allowed to circulate for 6 h for the nanoshells to localize in the tumor before the mouse was anaesthetized for imaging. As a comparison between antibody functionalized and nonfunctionalized gold nanoshells, 150 μl of anti-EGFR conjugated gold nanoshells with a concentration of 9.0×10^{10} particles/ml were also injected into the tail vein and allowed to circulate for 2 and 6 h prior to imaging to investigate and compare their longitudinal accumulation in tissue. For each of the test conditions, the OCT measurements were performed in triplicates, i.e., n = 3.

The commercial OCT system from Bioptigen, Incorporated (Durham, North Carolina) was used in this study and the system schematic is shown in Fig. 1. This portable system is described in more detail in our previous paper.[50] During the imaging procedure, the skin covering the tumor was removed to create an open tumor window that allowed the underlying tumor and the tumor-skin interface to be imaged (Fig. 1). The normal skin adjacent to the tumor was also imaged as a reference. A coverslip was positioned on top of the exposed tumor to remove the uneven contour for imaging. The space in-between was immersed in glycerol to provide index matching to reduce specular reflective artifact at the tissue-glass, interface. The OCT probe was placed directly on top of the coverslip and the tumors were vertically positioned and imaged with the top surface of the coverslip at 200 μm from the top of the OCT image screen for standardization. The scanning was done under B-mode imaging with 1000 axial A-scans to give an overall lateral scan range of 6 mm per B-scan frame; the imaging depth was about 1.5 mm. All the 1000 columns of axial A-scans from each B-scan were also averaged to obtain an average A-scan profile. As each test condition was performed in triplicate, i.e., n = 3, the A-scan profile for each mouse measurement was further averaged to obtain the mean A-scan profile of the triplicates for further analysis. All parameters including focus position and software constants remained the same throughout the entire study.

2.4 Tumor Tissue Examination for Gold Nanoshells

The imaged tumor tissues were examined for gold nanoshells using hematoxylin and eosin staining and confocal reflectance microscopy. Cryosections of 10 μm thickness at the site of imaging were obtained using a microtome cryostat (Cryo-Star HM 560MV, Germany), and the tissue sections were mounted onto slides. Sections were then counterstained with either eosin alone or a combination of Harris' hematoxylin and eosin, dehydrated in ascending grades of alcohol, mounted onto a coverslip with DePex as the mounting medium, and sealed with nail varnish prior to imaging. Images from the slides were obtained using the Olympus CK40 microscope with a 20× objective, and were captured in brightfield mode using the image processing software (Kontron KS400, version 3.0, Hallbergmoos, Germany). For confocal reflectance microscopy, the sectioned tissues were imaged using a laser scanning confocal microscope (Carl Zeiss LSM510 Meta) under confocal reflectance mode with an Olympus 20× objective. The confocal reflectance microscopy was performed under 633-nm excitation with a helium neon laser.

2.5 Image Data Analysis

The data from the OCT imaging were output to a computer for digital processing using the proprietary InVivoVue OCT software suite (Bioptigen Incorporated, Durham, North Carolina) to obtain the OCT individual A- and B-scan images. The 2-D B-scan images of 784 × 468 pixels were obtained by scanning the single-mode optical beam laterally over the sample, as described earlier. A custom routine was written in Matlab to further process the OCT image file offline to obtain the average A-scans for subsequent analysis and extraction of the μ_s of the imaged sample.

The multiple scattering theoretical OCT model based on the extended Huygens-Fresnel (EHF) theory was used to fit the measured average A-scan profile to extract the μ_s of the tissue under measurement.[52] This model accounts for both single and multiple scatterings in the sample, and is thus able to fit well into the average A-scan profile for a wide range of μ_s, including those used in this study. The curve-fitting process utilized a nonlinear least square fit of the data. For fitting
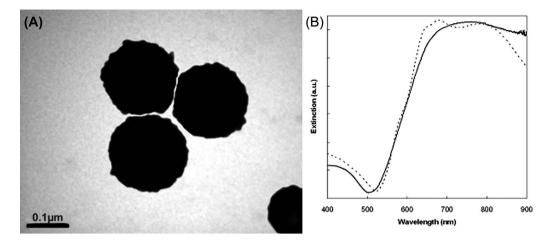
Fig. 2 (a) Electron micrograph of gold nanoshells with an 81-nm radius dielectric silica nanoparticle core and 23-nm-thick gold shell. (b) Measured UV-VIS extinction spectrum of the synthesized gold nanoshells (solid line). The theoretically calculated extinction spectrum of gold nanoshells of the same dimension as derived from the Mie theory is shown for comparison (dotted line).

of gold nanoshells in tumor tissue, the anisotropy factor g was set to 0.7 (Ref. 50)(θ_{rms}=0.77) for all cases. This is the anisotropy factor of tumor tissue that is the dominant scatterer used in the study. The anisotropy factor of gold nanoshells (g=0.0004) was not considered in the fitting, as the volume fraction of gold nanoshells used in our study, i.e., 0.0004 [based on the highest gold nanoshell concentration of 8.5×10^{10} particles/ml in 113 mm^3 of tumor (5 mm radius) after intratumoral injection] is too small to cause a substantial change in the overall scattering angle when added into tissue. However, to ascertain this would require a separate theoretical and experimental treatment, which would be beyond the scope of this study. In any case, the fitting of the theoretical OCT model appears rather insensitive to a range of anisotropy, as the R^2 value for the curve fitting does not vary much when the anisotropy is varied.

Since the system parameters such as the focal length, beam waist, source wavelength and refractive index of the sample are known *a priori*, the fitting process only involved μ_t. It is also known that the total sample extinction coefficient is the sum of the absorption and scattering coefficient, i.e., $\mu_t = \mu_a + \mu_s$. For most tissues, the absorption is often assumed to be negligible, i.e., $\mu_t \approx \mu_s$, since the intrinsic tissue absorption is known to be very small around the source wavelength. Hence, the OCT depth-dependent average A-scan has been modeled as a function of the scattering coefficient μ_s of the medium instead of μ_t.

3 Results

3.1 Optical Properties of Gold Nanoshells

The TEM image and measured UV-VIS extinction spectrum of the synthesized gold nanoshells are shown in Fig. 2. The measured spectrum shows that the 162-nm-diam silica core with 23-nm gold layer nanostructure produces a peak in its surface plasmon resonance at 765 nm, which is close to the operating wavelength of our OCT system to generate a large optical extinction in the gold nanoshells when excited by our light source. We note that the measured spectrum generally agrees well with the theoretical spectrum, although spectral broadening in the measured spectrum is observed. This may be attributed to the heterogeneity within a small population of gold nanoshells due to size variation in the silica core (typically about 4 % in our synthesis process[49]), as well as the differences in surface roughness and thickness of the shell formed.

3.2 Changes in Optical Contrast with Different Delivery Modes

For our *in vivo* study, we first show the observable changes in the optical contrast of tumor tissue when gold nanoshells are delivered via two different delivery modes into the tumor: intratumoral and IV. These two delivery modes deliver different amounts of gold nanoshells to the tumor, which would be useful to illustrate the difference in contrast enhancement arising from different gold nanoshell concentrations in tumors. The OCT images in Fig. 3(a) were acquired at the interface
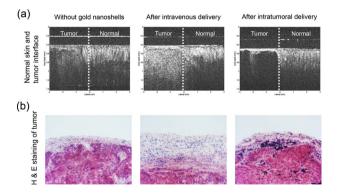

Fig. 3 (a) OCT images of the interface between normal peripheral skin and tumor tissue of mouse model prior to and after IV and intratumoral gold nanoshell delivery. The horizontal reflective surface shown on top of the tissue arises from the coverslip used to remove the uneven tissue contour for imaging. (b) Histological tissue sections of the tumor after HE staining for tumor without gold nanoshells (left), and tumor post-IV (middle) and intratumoral (right) gold nanoshell delivery. The HE stained tissue sections show the presence of gold nanoshells in the tumor tissue. Images were acquired with a 20× objective.
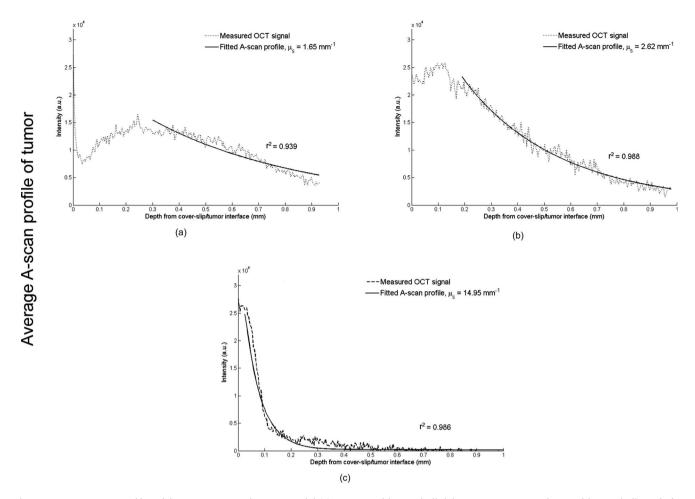
Average A-scan profile of tumor

(a)

(b)

(c)

Fig. 4 Average A-scan profiles of the tumor tissue of mouse model (a) prior to gold nanoshell delivery, i.e., tumor without gold nanoshells and after (b) IV and (c) intratumoral delivery of 150-μl pegylated gold nanoshells (9.0×10^{10} particles/ml) colloid. The measured OCT signal is shown by the dotted line, while the nonlinear least square fit of the data based on the multiple scattering EHF theory is shown by the solid line superimposed, giving an extracted μ_s of the composite gold nanoshells in tumor tissue of (a) 1.65 mm^{-1}, (b) 2.62 mm^{-1}, and (c) 14.95 mm^{-1}. In all three fittings, the coefficient of determination, $r^2 > 0.90$.

between the tumor and surrounding normal skin tissue. Compared to tumor tissue in the absence of gold nanoshells, a large concentration of gold nanoshells in the tumor arising from intratumoral injection shows at least two distinct changes in the OCT image. First, the OCT signal attenuates rapidly with depth to result in a loss of image brightness deeper into the tissue. This is accompanied by a signal intensity enhancement at the tissue surface. The overall visual effect is a bright but narrow signal band at the sample surface atop a dark region, arising from the highly attenuated OCT signal.

However, for a moderate concentration of gold nanoshells in tumor after IV delivery, the visibility of the tumor is improved, as the OCT signal intensity from the tumor is generally increased more uniformly with depth with smaller signal attenuation, with depth into the tissue. In addition to improvement in tumor visibility, the OCT images also show that the tumor margin between the tumor and adjacent normal skin tissue is also more clearly demarcated.

The histological tissue sections corresponding to the OCT images acquired from the same scanned site of the tumor are shown in Fig. 3(b). The tissue sections after HE staining show

the location of the gold nanoshells in the tumor tissue. Despite their nanoscale size, which is beyond the resolution limit of a conventional light microscope, the sudden intratumoral bolus injection of gold nanoshells causes them to be concentrated and closely spaced in the tumor tissue where they become observable collectively under the light microscope. With a slower delivery of gold nanoshells to the tumor via IV, the amount of gold nanoshells that localizes in the tissue is smaller and their presence in tumor can hardly be discerned visually from the tissue section.

3.3 Determination of Tissue μ_s and Gold Nanoshell Concentration in Tumor

The changes observed in the OCT image under different modes of gold nanoshell delivery described before can be characterized by changes to the scattering coefficient μ_s of the tumor tissue, which in turn can be extracted from the average OCT A-scans of the tissue. The average A-scan profile of the tumors prior to and after IV and intratumoral delivery of gold nanoshells is shown in Fig. 4. Compared to the average A-scan profile of tumor tissue alone, the presence of gold

nanoshells in tumor after IV delivery causes an increase in the OCT signal intensity, mainly at the top 300 μm of sample, while the signal attenuation as given by the slope of the depth-dependent OCT signal becomes more pronounced. This attenuation is relatively small compared to that after intratumoral delivery, where the large concentration of gold nanoshells in the tumor causes the signal in the average A-scan to attenuate rapidly with depth.

The average A-scan profiles allow the extraction of overall $\mu_{s,\text{GNS in tumor}}$ of the tumor with embedded gold nanoshells (GNS in tumor) by means of a nonlinear least square curve fitting of the theoretical OCT model.[52] The $\mu_{s,\text{GNS}}$ contributed by gold nanoshells alone in the tumor can then be derived simply by subtracting the $\mu_{s,\text{tumor}}$ of tumor tissue from $\mu_{s,\text{GNS in tumor}}$[53] according to the following equation: $\mu_{s,\text{GNS}} = \mu_{s,\text{GNS in tumor}} - \mu_{s,\text{tumor}}$. The result of curve fitting on the average A-scan profiles in Fig. 4 shows that the extracted $\mu_{s,\text{tumor}}$ of tumor tissue without gold nanoshells is 1.65 ± 0.73 mm^{-1}, while the extracted overall μ_s of tumor after IV and intratumoral delivery of gold nanoshells, i.e., are 2.62 ± 0.23 mm^{-1} and 14.95 ± 0.65 mm^{-1}, respectively. The postsubtraction $\mu_{s,\text{GNS}}$ contributed by gold nanoshells alone in tumor after IV and intratumoral delivery is then calculated to be 0.97 and 13.30 mm^{-1} respectively.

The extracted μ_s contributed by gold nanoshells alone further allows its concentration in the tumor to be deduced through the following theoretical relationship:

$$\mu_s = cAQ_{\text{sca}},$$

where c is the concentration of our synthesized gold nanoshells in particles/ml, A is its geometric cross section, and Q_{sca} is the scattering efficiency. This linear relationship assumes an independent scattering approximation. With a constant gold nanoshell size configuration (81-nm core radius and 23-nm shell thickness) of $A = 3.40 \times 10^{-14}$ m^2 used in this study, and a Q_{sca} of 4.58 at 840 nm based on theoretical calculations, μ_s scales linearly with concentration and the relationship can be further simplified to:

$$\mu_s = 1.556c \times 10^{-10} \text{ mm}^{-1}.$$

This linear relationship allows for an estimate of any unknown concentration of gold nanoshells in tissue given its extracted μ_s. Based on the linear relationship described before, the gold nanoshell concentration in the tumor after IV and intratumoral delivery is approximately 6.2×10^9 and 8.5×10^{10} particles/ml, which is equivalent to 6.9 and 94.4% of the injected gold nanoshell concentration, respectively.

3.4 Changes in Optical Contrast with Gold Nanoshell Concentration

In most cases of imaging, the contrast agent is usually injected intravenously instead of directly into the tissue of interest, since the locality of the diseased site is usually unknown. We thus extend the study on IV delivery to further demonstrate that intravenous control of optical contrast in tumors is possible by varying the concentration of gold nanoshells (1.1×10^{10} to 9.0×10^{10} particles/ml) injected. The OCT images of the tumor together with its corresponding

average A-scan profiles after 6 h of vascular circulation with different gold nanoshells concentration are shown in Fig. 5.

The OCT images in Fig. 5(a) show a gradual increase in the signal intensity, especially at the top 300-μm region, as the concentration of gold nanoshells injected increases. The signal attenuation with depth also becomes more pronounced with increasing concentration. These changes are similarly observed in the corresponding average A-scan profiles [Fig. 5(b)], where the negative slope of the depth-dependent A-scan curve increases, together with an increase in the OCT signal intensity at the more superficial region. The corresponding histological tissue sections acquired at the site of imaging and stained with eosin alone [Fig. 5(c)] show an increasing amount of gold nanoshells in the tumor tissue as more gold nanoshells are administered. Here, the gold nanoshells localize in the tumor tissue during the period of vascular circulation to form small random dark specks that are scattered over the eosin-stained tissue. These dark specks are possibly due to the presence of a collective population of the gold nanoshells in the tissue environment. The confocal reflectance images of the tissue sections [Fig. 5(d)] acquired at the same site as the histology also show the pseudocolored red reflectance arising from the gold nanoshells scattered with the increasing amount in tissue.

The extracted μ_s of gold nanoshell-laden tumor as determined from the theoretical curve fit of the average A-scan profile for different gold nanoshells concentrations, i.e., $\mu_{s,\text{GNS in tumor}}$, is indicated in Fig. 5(b) and summarized in Table 1. The postsubtraction $\mu_{s,\text{GNS}}$ contributed by gold nanoshells alone in tumor shows that the scattering coefficient attributed to gold nanoshells and its estimated tumor concentration exhibit a positive correlation with the injected concentration, although the relationship does not scale linearly with the amount of gold nanoshells injected as shown in Fig. 6. However, when the estimated gold nanoshell concentration in the tumor is expressed as a fraction of the injected concentration, we observe that this fractional concentration actually decreases with increasing injected concentration. Likewise, this negative correlation does not scale linearly to the injected concentration. As the injected concentration increases eightfold from 1.1×10^{10} to 9.0×10^{10} particles/ml, the fractional concentration of injected gold nanoshells that localizes in the tumor merely decreases about four-fold from 24.0 to 6.9%.

3.5 Antibody Surface Functionalization of Gold Nanoshells

The fractional concentration of injected gold nanoshells delivered to the tumor can be increased with appropriate surface functionalization on the gold nanoshells in the form of antibody conjugation. This introduces additional interaction between the gold nanoshells and the cells, thereby altering the dynamics of gold nanoshells reaching the tumor and hence facilitating the control of optical contrast of tumors. The anti-EGFR conjugated gold nanoshells were injected into the circulation of mice at a concentration of 9.0×10^{10} particles/ml and allowed to circulate in the blood before OCT images of tumor were acquired after 2 and 6 h of circulation. The pegylated gold nanoshells without antibody functionalization were also injected with the same dosage in separate mice, and monitored as a control for comparison.
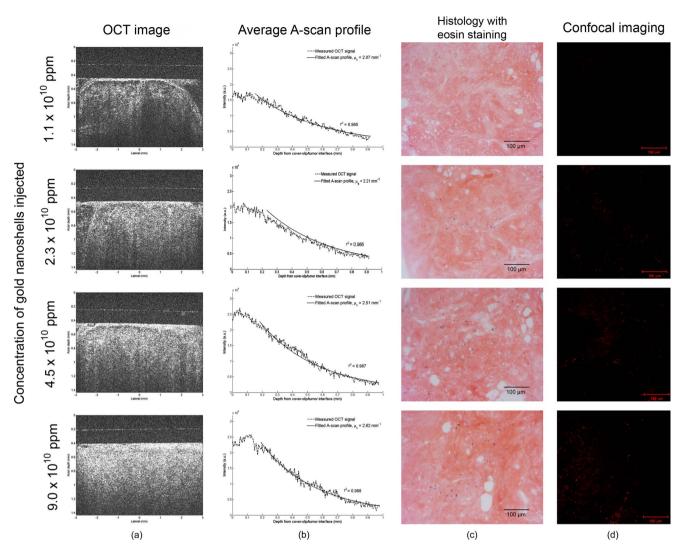
Fig. 5 Changes in the (a) OCT image, (b) average A-scan profile, (c) histological tissue section with eosin staining, and (d) confocal reflectance image of mouse tumor tissue after 6 h of vascular circulation for a range of gold nanoshell concentration (1.1×10^{10} to 9.0×10^{10} particles/ml) injected intravenously. In the average A-scan profile in (b), the measured OCT signal is shown by the dotted line, while the nonlinear least square fit of the data is shown by the solid line superimposed with the extracted μ_s. Both the histological and confocal images were acquired under a 20× objective. The confocal reflectance microscopy was performed under 633-nm excitation.

The OCT images in Fig. 7(a) show that the signal intensity at both 2 and 6 h for tumor loaded with anti-EGFR gold nanoshells is generally higher, especially in regions nearer to the tissue surface compared to tumor loaded with pegylated gold nanoshells, with the difference being more obvious at 2-h time point. In addition, the change in optical contrast of tumor from 2 to 6 h is observable for both types of gold nanoshells, although the longitudinal signal change seems more apparent for the pegylated gold nanoshells compared to the anti-EGFR conjugated gold nanoshells. In the case of pegylated gold nanoshells, the increase in optical contrast compared to tumor without gold nanoshells is hardly observable at 2 h, and would require another 4 h of circulation before the optical effect brought about by the gold nanoshells could be observed clearly. This is unlike the case of anti-EGFR conjugated gold nanoshells, where the increase in optical contrast is already observable after 2 h and it continues to increase, albeit more slowly, during the next 4 h.

The average A-scan corresponding to the OCT images in Fig. 7(b) shows the nonlinear least square fit of the theoretical curve over the tumor data and the extracted $\mu_{s,\text{GNS in tumor}}$ for all four instances in Fig. 7. From the postsubtraction $\mu_{s,\text{GNS}}$, the gold nanoshell concentration in tumor is derived as shown in Table 2. The results show that the concentration of pegylated gold nanoshells is estimated to increase from 2.6 $\times10^8$ particles/ml at 2 h to 6.2×10^9 particles/ml at 6 h. This represents a 24-fold increase in the fractional concentration from 0.29 to 6.9% of the injected gold nanoshell concentration. In comparison, the estimated concentration of anti-EGFR conjugated gold nanoshells in tumor is higher at both time points and it increases from 4.9×10^9 particles/ml at 2 h to 7.4×10^9 particles/ml at 6 h. Despite having a higher concentration of gold nanoshells in tumor at both time points, the fractional concentration of injected anti-EGFR conjugated gold nanoshells that localizes in the tumor over the 4 h inter-

Table 1 Summary of extracted $\mu_{s,\text{GNS in tumor}}$ of gold nanoshell laden tumor as determined from the theoretical curve fit of average A-scan profile, as well as the estimated gold nanoshell concentration in tumor for different concentration of gold nanoshells injected intravenously. In all cases, the tumor tissue μ_s of 1.65 mm^{-1} is subtracted from $\mu_{s,\text{GNS in tumor}}$ to obtain the $\mu_{s,\text{GNS}}$ due to gold nanoshells alone.

Concentration of gold nanoshells injected (particles/ml)	Extracted $\mu_{s,\text{GNS in tumor}}$ (mm^{-1})	Postsubtraction $\mu_{s,\text{GNS}}$ (mm^{-1})	Estimated gold nanoshell concentration in tumor (particles/ml)	Fractional concentration of injected gold nanoshells that localize in tumor
1.1×10^{10}	2.07 ± 0.30	0.42	2.7×10^{9}	24.0%
2.3×10^{10}	2.21 ± 0.31	0.56	3.6×10^{9}	16.0%
4.5×10^{10}	2.51 ± 0.25	0.86	5.5×10^{9}	12.3%
9.5×10^{10}	2.62 ± 0.34	0.97	6.2×10^{9}	6.9%

val increases by a smaller amount from 5.5% at 2 h to 8.2% at 6 h of circulation.

4 Discussion

The optical characterization of OCT has been studied by several groups, and a few theoretical models have been established to relate the sample optical parameters to their corresponding A-scan profile[52,54,55] with the aim to extract out the parameters for diagnostic purposes such as diabetic glucose sensing.[56] Previous studies have shown that the negative gradient of the average A-scan profile is a function of μ_t.[57,58] As μ_t increases, the slope of the average A-scan profile also increases. Since biological tissues are known to be scattering dominant with negligible absorption, i.e., $\mu_a \approx 0$, the extracted $\mu_t \approx \mu_s$ of tissue. Therefore, the slope of the average A-scan profile determines the μ_s of the tissue being examined.

In the extraction of μ_s from the average A-scan profile, the importance of tissue homogeneity should not be understated. This is because the theoretical OCT model used to fit the A-scan profile was developed based on an optically homog-
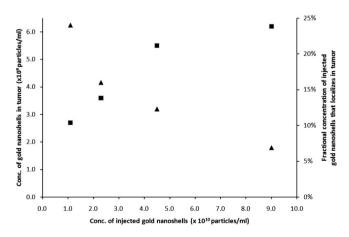
enous sample whose entire A-scan profile can be fitted by a single equation. Heterogeneous samples with multiple layers or regions of different μ_s would require multiple equations to fit different layers individually, thus rendering the single equation inappropriate. For this reason, the average A-scan profile of normal skin with multiple stromal layers of different μ_s was not fitted to extract its mean μ_s. The tumor tissue, on the other hand, is often assumed to possess homogenous optical properties.[59] Therefore, we were able to extract the μ_s of tumor tissue with a good degree of fit (coefficient of determination, $r^2 = 0.94$). In fact, the rest of the average A-scans in our small animal imaging were also well fitted with $r^2 > 0.97$ to provide an accurate extraction of μ_s.

The subtraction of $\mu_{s,\text{GNS in tumor}}$ to obtain $\mu_{s,\text{GNS}}$ allows the concentration of gold nanoshells in tumor tissue to be estimated as described earlier. Here, we would like to comment that the mathematically derived $\mu_{s,\text{GNS}}$ assumes that the optical absorption in gold nanoshells is small, such that the $\mu_{t,\text{GNS}}$ approximates its $\mu_{s,\text{GNS}}$, as in the case of biological tissue. This is true given that the gold nanoshells of this size configuration are predominantly scattering as determined from the Mie theory (results not shown). Futhermore, in the subtraction of $\mu_{s,\text{GNS in tumor}}$ to obtain $\mu_{s,\text{GNS}}$, the scattering coefficient of tumor $\mu_{s,\text{tumor}}$ of 1.65 mm^{-1} (Fig. 4) is used in all the analysis throughout this study. This value concurs with those reported in the literature[60,61] and is used, albeit with the caution that small variations in the scattering coefficients of tumor tissue do exist, which may affect the computation of the gold nanoshell concentration.

In calculating the concentration of gold nanoshells in tissue, we also assume that the gold nanoshells are monodisperse in size such that their geometric cross section and scattering efficiency is a constant in tissue. In reality, small variations in the size of the synthesized gold nanoshells do exist, and a small population of the gold nanoshells may be aggregated to varying degrees in tissue to result in changes to their optical properties. Such aggregation occurs despite prior successful pegylation *in vitro*[62] and could possibly be attributed to the inherent instability of the pegylation in the tissue interstitial environment arising from the weak gold-monothiol interaction between the gold surface and mPEG-thiol tether.

Fig. 6 Nonlinear relationship between the concentration of gold nanoshells localized in tumor and the injected gold nanoshell concentration (-■-). The tumor concentration of gold nanoshells expressed as a fractional concentration of the injected gold nanoshell concentration (-▲-) is also plotted.
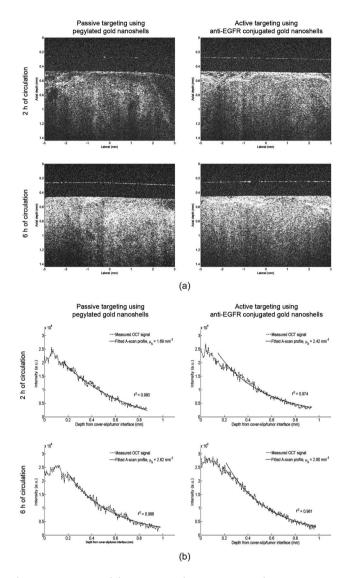
(a)

(b)

Fig. 7 Comparison of the OCT signal in tumor tissue between using nonfunctionalized pegylated gold nanoshells (left column) and anti-EGFR conjugated gold nanoshells (right column) showing the changes in (a) OCT images and (b) average A-scan profile after 2 h (top) and 6 h (bottom) of gold nanoshells (9.0×10^{10} particles/ml) IV delivery. In the average A-scan profile in (b), the measured OCT signal is shown by the dotted line, while the nonlinear least square fit of the data is shown by the solid line superimposed with the extracted μ_s shown in the figure.

Furthermore, the linear relationship between $\mu_{s,\mathrm{GNS}}$ and gold nanoshell concentration is limited. As previous studies with other particle scatterers such as Intralipid have shown, the relationship turns nonlinear at high particle concentrations due to interparticle shadowing effects.[63] Nonetheless, our previous studies on phantom models have shown that the derived $\mu_{s,\mathrm{GNS}}$ appear to deviate only slightly from the theoretical linearity at very high concentrations.[50] This linear region is thus sufficiently wide to allow an accurate gold nanoshell concentration to be determined over a wide range, which includes that used in this study.

Keeping in mind the various limitations discussed before, the deduced gold nanoshell concentration from the $\mu_{s,\mathrm{GNS}}$ is therefore only an approximation that is subjected to the vari-

ous physical properties of gold nanoshells, e.g., size variations, state of aggregation, and their concentration in tissue as discussed. Further evaluation of the accuracy of this noninvasive approach in determining the gold nanoshell concentration in tissue would warrant a separate study that would allow comparison with another independent invasive technique such as inductively coupled plasma mass spectroscopy (ICPMS). Nonetheless, such a noninvasive approach in determining the gold nanoshells concentration in tissue holds possible applications in biodistribution studies, and could potentially allow rapid concentration mapping of gold nanoshells in tissue for quantitative molecular imaging of certain crucial biomarkers associated with cancer, particularly in cases where the vitality of the animal subject is crucial.

In this study, we observe that different concentrations of gold nanoshells in tumor tissue would produce different outcomes on the OCT contrast enhancement, as depicted by the two delivery modes. Both of the delivery modes, i.e., intratumoral and IV, are commonly used to deliver therapeutic compounds to the target site of interest, which is the tumor in this case. In intratumoral delivery, the bolus injection of a 9.0×10^{10} particles/ml dosage of gold nanoshells directly into the tumor causes a high concentration ($\approx 8.5 \times 10^{10}$ particles/ml) to localize there, which works out to 94.4% of the injected gold nanoshell concentration.

With a large concentration of gold nanoshells, the incident light from OCT that enters the tumor experiences higher levels of scattering near the surface due to the presence of gold nanoshell scatterers. The higher concentration of particle scatterers also causes a larger amount of single backscattered light that collectively contributes to the overall backscattered light from tissue. These account for the strong OCT signal enhancement near the tissue surface as observed in our results. With a large fraction of incident light backscattered out of the tissue, the amount of light that reaches deeper into the tissue is reduced, giving rise to a significant signal attenuation with depth.

On the other hand, the delivery of the same dose by IV results in a much lower concentration of gold nanoshells ($\approx 6.2 \times 10^9$ particles/ml) in the tumor site via the enhanced permeation and retention (EPR) effect. This estimated concentration is only about 6.9% of the injected gold nanoshell concentration. The reason for a much lower tumor concentration of gold nanoshells with IV delivery is because a significant amount of injected gold nanoshells is either lost from the bloodstream during circulation due to renal excretion, or removed by the reticulo-endothelial system (RES). Despite their pegylation, the removal of gold nanoshells by RES is inevitable, although pegylation does help to minimize the RES uptake.[62] The instability of the gold-monothiol interaction between the gold surface and mPEG-thiol tether as mentioned earlier may have also contributed toward the RES uptake after prolonged circulation in the biological environment.

With a smaller concentration of gold nanoshells, the incident light from the OCT that enters the tumor experiences a longer mean free path, thus allowing a larger fraction of incident light to reach deeper into the tissue and reduce the signal attenuation with depth. Consequently, the amount of single backscattered light from regions near the tissue surface is reduced, thus giving a weaker signal enhancement. Throughout

Table 2 Summary of extracted $\mu_{s,GNS\ in\ tumor}$ of gold nanoshell laden tumor as determined from the theoretical curve fit of average A-scan profile, $\mu_{s,GNS}$ of gold nanoshells in tumor postsubtracting μ_s of tumor tissue, i.e. 1.65 mm^{-1}, and estimated gold nanoshell concentration in tumor after 2 and 6 h of vascular circulation with nonspecific pegylated and anti-EGFR conjugated gold nanoshells.

Type of gold nanoshells injected	Blood circulation period	Extracted $\mu_{s,GNS\ in\ tumor}$ (mm^{-1})	Postsubtraction $\mu_{s,GNS}$ (mm^{-1})	Estimated gold nanoshell concentration in tumor (particles/ml)	Fractional concentration of injected gold nanoshells that localize in tumor
Pegylated gold nanoshells	2 h	1.69 ± 0.27	0.04	2.6×10^8	0.29%
	6 h	2.62 ± 0.34	0.97	6.2×10^9	6.9%
Anti-EGFR conjugated gold nanoshells	2 h	2.42 ± 0.23	0.77	4.9×10^9	5.5%
	6 h	2.80 ± 0.25	1.15	7.4×10^9	8.2%

the study, it is noteworthy that the injected gold nanoshells also seem to cause an observable change to the OCT signal intensity of the surrounding normal tissue. This is unavoidable, given the poor specificity of passive targeting. However, such an increase in the OCT signal intensity in normal tissue cannot be easily and meaningfully quantified and compared to the increase in tumor, as it would require a separate detailed study on the tumor-to-normal ratio, which is beyond the scope of this study that only aims to characterize the OCT signal increase in tumor tissue.

The observable changes in OCT image and average A-scan profile for increasing concentration of gold nanoshells in the tumor agree well with the results of our previous phantom studies.[50] The effect of an increasing gold nanoshell concentration on the OCT signal holds an important implication to the dosing of these nanoparticulate contrast agent to control the OCT image contrast enhancement in living systems, as an appropriate dosing regime is crucial in achieving a good compromise between OCT signal enhancement at the surface region and minimal signal attenuation deeper in the tissue. As the gold nanoshell dosage increases, the data seem to suggest a limiting concentration of gold nanoshells in the tumor beyond the 6-h time point. Thus, higher dosing may not necessarily be more effective in delivering a larger amount of gold nanoshells to the tumor site, since a smaller fractional concentration of injected gold nanoshells actually localizes in the tumor.

Our results have also shown that the use of antibody surface functionalization is one strategy that can improve the uptake of gold nanoshells in tumor. In this study, the overexpression of EGFR on the surface of tumor forming cancer cells is used as a cancer marker, and the anti-EGFR is suppose to guide the gold nanoshells to the EGFR tumor marker. The A-431 cells that were inoculated to form the xenograft tumor in mice are widely known to have an expression of EGFR that is several times higher than normal cells. This high expression of EGFR, together with a relatively porous tumor vasculature, facilitates receptor-ligand interaction that would encourage more gold nanoshells to localize in the tumor. However, it is also very likely that the presence of the antibody protein in-creases the nonspecific adhesion of the gold nanoshells to the tissue, thus causing an increase in tumor uptake. Therefore, it would be hard to verify that the mechanism for this increased tumor uptake is due to antibody-specific targeting based solely on the results of this study, where the previously mentioned nonspecific uptake has not been investigated.

In any case, both the nonfunctionalized pegylated gold nanoshells and the antibody conjugated gold nanoshells rely on vascular porosity to confer a moderate level of tumor specificity, while the antibody conjugated gold nanoshells offer additional cellular interaction to enable greater gold nanoshell uptake in tumor. This by itself would be sufficient to explain the increase in absolute as well as fractional concentration of injected gold nanoshells that localize in the tumor at both time points compared to pegylated gold nanoshells.

Apart from a greater concentration of gold nanoshells in tumor, antibody surface functionalization also tends to accelerate the rate of gold nanoshells reaching the tumor, which explains the significant difference in the OCT image brightness between that of nonfunctionalized pegylated gold nanoshells and antibody conjugated gold nanoshells at 2 h. This arises because the EPR effect is a slow biological process of transporting gold nanoshells out of the vasculature into the tumor. This slow transport coupled with a weak interaction with the tumor tissue, which tend to discourage its accumulation there, would therefore require a longer period of vascular circulation, i.e., 6 h before a sufficient amount of pegylated gold nanoshells are localized to cause an observable change in the OCT image. The antibody conjugated gold nanoshells eliminate this problem by having a stronger interaction with the tumor tissue to allow more gold nanoshells to localize and accumulate in tumor within a shorter time of 2 h.

However, given more time for the pegylated gold nanoshells to passively localize in the tumor, the difference in the OCT image at 6 h is reduced. This occurs as the pegylated gold nanoshells accumulate continuously in the tumor, while the rate of anti-EGFR conjugated gold nanoshell delivery to tumor reduces, as more of them accumulate in the tumor after 6 h and the diffusion transport gradient is reduced. For the

same reason, the longitudinal change in OCT image and average A-scan profile between 2 and 6 h is more apparent for pegylated gold nanoshells compared to anti-EGFR conjugated gold nanoshells, since the former require a longer period of 6 h before they localize sufficiently to produce an observable contrast, while the latter localize sufficiently fast within 2 h to produce the same observable contrast. Such delivery dynamics hold considerable implications toward developing a contrasting regime where time is crucial to the subject being studied.

5 Conclusion

We demonstrate the *in vivo* control of optical contrast in a mouse xenograft tumor model using gold nanoshells as a contrast agent in OCT. This is achieved via three approaches: 1. employing different modes of gold nanoshells delivery such as intratumoral or IV, 2. varying the concentration of the injected dose, and 3. enabling antibody surface functionalization on gold nanoshells. With appropriate dosing, IV delivery results in a gold nanoshell concentration in tumor that achieves a good compromise in enhancing the OCT signal without significantly attenuating the signal deeper into the tissue. The concentration of gold nanoshells in the tumor tissue of live mice can be deduced using a noninvasive technique based on the theoretical modeling of OCT backscattering signal profile. We use this technique to examine the dynamics of gold nanoshells present in tumor with variations in intravenous-injected dosage and presence of surface functionalization. The results reveal a nonlinear response of gold nanoshell concentration in tumor with increasing dosage. The use of antibody functionalization on the gold nanoshells serves not just to improve this fractional concentration of injected gold nanoshells in tumor, but also hasten the delivery of nonfunctionalized pegylated gold nanoshells. Such insights enable us to understand better the dynamics of gold nanoshell tumor delivery and thereby hold several implications toward developing an optimized contrast protocol to add further value to the clinical significance of OCT.

References

1. D. Huang, E. A. Swanson, C. P. Lin, J. S. Schuman, W. G. Stinson, W. Chang, M. R. Hee, T. Flotte, K. Gregory, C. A. Puliafito et al., "Optical coherence tomography," *Science* **254** (5035), 1178–1181 (1991).
2. R. Weissleder, "A clearer vision for *in vivo* imaging," *Nat. Biotechnol.* **19**(4), 316–317 (2001).
3. J. G. Fujimoto, M. E. Brezinski, G. J. Tearney, S. A. Boppart, B. Bouma, M. R. Hee, J. F. Southern, and E. A. Swanson, "Optical biopsy and imaging using optical coherence tomography," *Nat. Med.* **1** 970–972 (1995).
4. M. R. Hee, J. A. Izatt, E. A. Swanson, D. Huang, J. S. Schuman, C. P. Lin, C. A. Puliafito, and J. G. Fujimoto, "Optical coherence tomography of the human retina," *Arch. Ophthalmol. (Chicago)* **113**(3), 325–332 (1995).
5. I. Cilesiz, P. Fockens, R. Kerindongo, D. Faber, G. Tytgat, F. Ten Kate, and T. Van Leeuwen, "Comparative optical coherence tomography imaging of human esophagus: how accurate is localization of the muscularis mucosae?" *Gastrointest. Endosc.* **56**(6), 852–857 (2002).
6. X. D. Li, S. A. Boppart, J. Van Dam, H. Mashimo, M. Mutinga, W. Drexler, M. Klein, C. Pitris, M. L. Krinsky, M. E. Brezinski, and J. G. Fujimoto, "Optical coherence tomography: advanced technology for the endoscopic imaging of Barrett's esophagus," *Endoscopy* **32**(12), 921–930 (2000).
7. G. J. Tearney, M. E. Brezinski, J. F. Southern, B. E. Bouma, S. A. Boppart, and J. G. Fujimoto, "Optical biopsy in human gastrointestinal tissue using optical coherence tomography," *Am. J. Gastroenterol.* **92**(10), 1800–1804 (1997).
8. K. Kobayashi, J. A. Izatt, M. D. Kulkarni, J. Willis, and M. V. Sivak, Jr., "High-resolution cross-sectional imaging of the gastrointestinal tract using optical coherence tomography: preliminary results," *Gastrointest. Endosc.* **47**(6), 515–523 (1998).
9. A. Sergeev, V. Gelikonov, G. Gelikonov, F. Feldchtein, R. Kuranov, N. Gladkova, N. Shakhova, L. Snopova, A. Shakhov, I. Kuznetzova, A. Denisenko, V. Pochinko, Y. Chumakov, and O. Streltzova, "*In vivo* endoscopic OCT imaging of precancer and cancer states of human mucosa," *Opt. Express* **1**(13), 432–440 (1997).
10. M. E. Brezinski, G. J. Tearney, B. E. Bouma, J. A. Izatt, M. R. Hee, E. A. Swanson, J. F. Southern, and J. G. Fujimoto, "Optical coherence tomography for optical biopsy. Properties and demonstration of vascular pathology," *Circulation* **93**(6), 1206–1213 (1996).
11. F. J. van der Meer, D. J. Faber, J. Perree, G. Pasterkamp, D. Baraznji Sassoon, and T. G. van Leeuwen, "Quantitative optical coherence tomography of arterial wall components," *Lasers Med. Sci.* **20**(1), 45–51 (2005).
12. J. G. Fujimoto, C. Pitris, S. A. Boppart, and M. E. Brezinski, "Optical coherence tomography: an emerging technology for biomedical imaging and optical biopsy," *Neoplasia* **2**(1–2), 9–25 (2000).
13. S. A. Boppart, B. E. Bouma, C. Pitris, J. F. Southern, M. E. Brezinski, and J. G. Fujimoto, "*In vivo* cellular optical coherence tomography imaging," *Nat. Med.* **4**(7), 861–865 (1998).
14. E. S. Matheny, N. M. Hanna, W. G. Jung, Z. Chen, P. Wilder-Smith, R. Mina-Araghi, and M. Brenner, "Optical coherence tomography of malignancy in hamster cheek pouches," *J. Biomed. Opt.* **9**(5), 978–981 (2004).
15. A. V. D'Amico, M. Weinstein, X. Li, J. P. Richie, and J. Fujimoto, "Optical coherence tomography as a method for identifying benign and malignant microscopic structures in the prostate gland," *Urology* **55**(5), 783–787 (2000).
16. G. J. Tearney, M. E. Brezinski, B. E. Bouma, S. A. Boppart, C. Pitris, J. F. Southern, and J. G. Fujimoto, "*In vivo* endoscopic optical biopsy with optical coherence tomography," *Science* **276** (5321), 2037–2039 (1997).
17. J. K. Barton, K. W. Gossage, W. Xu, J. R. Ranger-Moore, K. Saboda, C. A. Brooks, L. D. Duckett, S. J. Salasche, J. A. Warneke, and D. S. Alberts, "Investigating sun-damaged skin and actinic keratosis with optical coherence tomography: a pilot study," *Technol. Cancer Res. Treat.* **2**(6), 525–535 (2003).
18. A. R. Tumlinson, L. P. Hariri, U. Utzinger, and J. K. Barton, "Miniature endoscope for simultaneous optical coherence tomography and laser-induced fluorescence measurement," *Appl. Opt.* **43**(1), 113–121 (2004).
19. S. Jackle, N. Gladkova, F. Feldchtein, A. Terentieva, B. Brand, G. Gelikonov, V. Gelikonov, A. Sergeev, A. Fritscher-Ravens, J. Freund, U. Seitz, S. Soehendra, and N. Schrodern, "*In vivo* endoscopic optical coherence tomography of the human gastrointestinal tract—toward optical biopsy," *Endoscopy* **32**(10), 743–749 (2000).
20. T. M. Yelbuz, M. A. Choma, L. Thrane, M. L. Kirby, and J. A. Izatt, "Optical coherence tomography: a new high-resolution imaging technology to study cardiac development in chick embryos," *Circulation* **106**(22), 2771–2774 (2002).
21. A. N. Bashkatov, E. A. Genina, Y. P. Sinichkin, and V. V. Tuchin, "The influence of glycerol on the transport of light in the skin," *Proc. SPIE* **4623**, 144–152 (2002)..
22. R. K. Wang and J. B. Elder, "Propylene glycol as a contrasting agent for optical coherence tomography to image gastrointestinal tissues," *Lasers Surg. Med.* **30**(3), 201–208 (2002).
23. C. Christiansen, H. Kryvi, P. C. Sontum, and T. Skotland, "Physical and biochemical characterization of Albunex, a new ultrasound contrast agent consisting of air-filled albumin microspheres suspended in a solution of human albumin," *Biotechnol. Appl. Biochem.* **19** (Pt 3) 307–320 (1994).
24. J. K. Barton, J. B. Hoying, and C. J. Sullivan, "Use of microbubbles as an optical coherence tomography contrast agent," *Acad. Radiol.* **9**

(Suppl 1) S52–S55 (2002).

25. T. M. Lee, A. L. Oldenburg, S. Sitafalwalla, D. L. Marks, W. Luo, F. J. Toublan, K. S. Suslick, and S. A. Boppart, "Engineered microsphere contrast agents for optical coherence tomography," *Opt. Lett.* **28**(17), 1546–1548 (2003).

26. A. M. Gobin, M. H. Lee, N. J. Halas, W. D. James, R. A. Drezek, and J. L. West, "Near-infrared resonant nanoshells for combined optical imaging and photothermal cancer therapy," *Nano Lett.* **7**(7), 1929–1934 (2007).

27. C. Loo, A. Lowery, N. Halas, J. West, and R. Drezek, "Immunotargeted nanoshells for integrated cancer imaging and therapy," *Nano Lett.* **5**(4), 709–711 (2005).

28. C. Loo, L. Hirsch, M. H. Lee, E. Chang, J. West, N. Halas, and R. Drezek, "Gold nanoshell bioconjugates for molecular imaging in living cells," *Opt. Lett.* **30**(9), 1012–1014 (2005).

29. C. Loo, A. Lin, L. Hirsch, M. H. Lee, J. Barton, N. Halas, J. West, and R. Drezek, "Nanoshell-enabled photonics-based imaging and therapy of cancer," *Technol. Cancer Res. Treat.* **3**(1), 33–40 (2004).

30. A. L. Oldenburg, M. N. Hansen, D. A. Zweifel, A. Wei, and S. A. Boppart, "Plasmon-resonant gold nanorods as low backscattering albedo contrast agents for optical coherence tomography," *Opt. Express* **14**(15), 6724–6738 (2006).

31. S. J. Oldenburg, J. B. Jackson, S. L. Westcott, and N. J. Halas, "Infrared extinction properties of gold nanoshells," *Appl. Phys. Lett.* **75**(19), 2897–2899 (1999).

32. K. J. Liu, M. W. Grinstaff, J. Jiang, K. S. Suslick, H. M. Swartz, and W. Wang, "*In vivo* measurement of oxygen concentration using sonochemically synthesized microspheres," *Biophys. J.* **67**(2), 896–901 (1994).

33. D. P. O'Neal, L. R. Hirsch, N. J. Halas, J. D. Payne, and J. L. West, "Photo-thermal tumor ablation in mice using near infrared-absorbing nanoparticles," *Cancer Lett.* **209**(2), 171–176 (2004).

34. Y. Matsumura and H. Maeda, "A new concept for macromolecular therapeutics in cancer chemotherapy: mechanism of tumoritropic accumulation of proteins and the antitumor agent smancs," *Cancer Res.* **46** (12 Pt 1), 6387–6392 (1986).

35. H. Maeda, J. Fang, T. Inutsuka, and Y. Kitamoto, "Vascular permeability enhancement in solid tumor: various factors, mechanisms involved and its implications," *Int. J. Immunopharmacol* **3**(3), 319–328 (2003).

36. W. D. James, L. R. Hirsch, J. L. West, P. D. O'Neal, and J. D. Payne, "Application of INAA to the build-up and clearance of gold nanoshells in clinical studies in mice," *J. Radioanal. Nucl. Chem.* **271** 455–459 (2007).

37. J. Chen, F. Saeki, B. J. Wiley, H. Cang, M. J. Cobb, Z. Y. Li, L. Au, H. Zhang, M. B. Kimmey, X. Li, and Y. Xia, "Gold nanocages: bioconjugation and their potential use as optical imaging contrast agents," *Nano Lett.* **5**(3), 473–477 (2005).

38. X. Huang, I. H. El-Sayed, W. Qian and M. A. El-Sayed, "Cancer cell imaging and photothermal therapy in the near-infrared region by using gold nanorods," *J. Am. Chem. Soc.* **128**(6), 2115–2120 (2006).

39. R. Goel, N. Shah, R. Visaria, G. F. Paciotti, and J. C. Bischof, "Biodistribution of TNF-alpha-coated gold nanoparticles in an *in vivo* model system," *Nanomedicine* **4**(4), 401–410 (2009).

40. M. P. Melancon, W. Lu, Z. Yang, R. Zhang, Z. Cheng, A. M. Elliot, J. Stafford, T. Olson, J. Z. Zhang, and C. Li, "*In vitro* and *in vivo* targeting of hollow gold nanoshells directed at epidermal growth factor receptor for photothermal ablation therapy," *Mol. Cancer Ther.* **7**(6), 1730–1739 (2008).

41. G. F. Paciotti, L. Myer, D. Weinreich, D. Goia, N. Pavel, R. E. McLaughlin, and L. Tamarkin, "Colloidal gold: a novel nanoparticle vector for tumor directed drug delivery," *Cancer Drug Deliv.* **11**(3), 169–183 (2004).

42. G. Zhang, Z. Yang, W. Lu, R. Zhang, Q. Huang, M. Tian, L. Li, D. Liang, and C. Li, "Influence of anchoring ligands and particle size on the colloidal stability and *in vivo* biodistribution of polyethylene glycol-coated gold nanoparticles in tumor-xenografted mice," *Biomaterials* **30**(10), 1928–1936 (2009).

43. J. C. Kah, R. C. Wan, K. Y. Wong, S. Mhaisalkar, C. J. Sheppard, and M. Olivo, "Combinatorial treatment of photothermal therapy using gold nanoshells with conventional photodynamic therapy to improve treatment efficacy: an *in vitro* study," *Lasers Surg. Med.* **40**(8), 584–589 (2008).

44. J. C. Kah, K. W. Kho, C. G. Lee, C. James, R. Sheppard, Z. X. Shen, K. C. Soo, and M. C. Olivo, "Early diagnosis of oral cancer based on

45. J. C. Kah, M. C. Olivo, C. G. Lee, and C. J. Sheppard, "Molecular contrast of EGFR expression using gold nanoparticles as a reflectance-based imaging probe," *Mol. Cell. Probes* **22**(1), 14–23 (2008).

46. W. Yasui, H. Sumiyoshi, J. Hata, T. Kameda, A. Ochiai, H. Ito, and E. Tahara, "Expression of epidermal growth factor receptor in human gastric and colonic carcinomas," *Cancer Res.* **48**(1), 137–141 (1988).

47. S. Costa, H. Stamm, A. Almendral, H. Ludwig, R. Wyss, D. Fabbro, A. Ernst, A. Takahashi, and U. Eppenberger, "Predictive value of EGF receptor in breast cancer," *Lancet* **2** (8622), 1258 (1988).

48. K. K. Ang, B. A. Berkey, X. Tu, H. Z. Zhang, R. Katz, E. H. Hammond, K. K. Fu, and L. Milas, "Impact of epidermal growth factor receptor expression on survival and pattern of relapse in patients with advanced head and neck carcinoma," *Cancer Res.* **62**(24), 7350–7356 (2002).

49. J. C. Y. Kah, N. Phonthammachai, R. C. Y. Wan, J. Song, T. White, I. Ahmad, C. Sheppard, and M. Olivo, "Synthesis of gold nanoshells based on the deposition-precipitation process," *Gold Bull.* **41**(1), 23–36 (2008).

50. J. C. Kah, T. H. Chow, B. K. Ng, S. G. Razul, M. Olivo, and C. J. Sheppard, "Concentration dependence of gold nanoshells on the enhancement of optical coherence tomography images: a quantitative study," *Appl. Opt.* **48**(10), D96–D108 (2009).

51. C. F. Bohren and D. R. Huffman, *Absorption and Scattering of Light by Small Particles*, Wiley-Interscience, New York (1998).

52. L. Thrane, H. T. Yura, and P. E. Andersen, "Analysis of optical coherence tomography systems based on the extended Huygens-Fresnel principle," *J. Opt. Soc. Am. A Opt. Image Sci. Vis* **17**(3), 484–490 (2000).

53. A. W. Lin, N. A. Lewinski, J. L. West, N. J. Halas, and R. A. Drezek, "Optically tunable nanoparticle contrast agents for early cancer detection: model-based analysis of gold nanoshells," *J. Biomed. Opt.* **10**(6), 064035 (2005).

54. A. I. Kholodnykh, I. Y. Petrova, K. V. Larin, M. Motamedi, and R. O. Esenaliev, "Precision of measurement of tissue optical properties with optical coherence tomography," *Appl. Opt.* **42**(16), 3027–3037 (2003).

55. T. G. van Leeuwen, D. J. Faber, and M. C. Aalders, "Measurement of the axial point spread function in scattering media using single-mode fiber-based optical coherence tomography," *IEEE J. Sel. Top. Quantum Electron.* **9**(2), 227–233 (2003).

56. R. O. Esenaliev, K. V. Larin, I. V. Larina, and M. Motamedi, "Noninvasive monitoring of glucose concentration with optical coherence tomography," *Opt. Lett.* **26**(13), 992–994 (2001).

57. J. A. Izatt, M. R. Hee, G. M. Owen, E. A. Swanson, and J. G. Fujimoto, "Optical coherence microscopy in scattering media," *Opt. Lett.* **19**(8), 590–592 (1994).

58. D. Faber, F. van der Meer, M. Aalders, and T. van Leeuwen, "Quantitative measurement of attenuation coefficients of weakly scattering media using optical coherence tomography," *Opt. Express* **12**(19), 4353–4365 (2004).

59. R. T. Zaman, P. Diagaradjane, J. C. Wang, J. Schwartz, N. Rajaram, K. L. Gill-Sharp, S. H. Cho, H. G. Rylander, J. D. Payne, S. Krishnan, and J. W. Tunnell, "*In vivo* detection of gold nanoshells in tumors using diffuse optical spectroscopy," *IEEE J. Sel. Top. Quantum Electron.* **13**(6), 1715–1720 (2007).

60. A. L. Clark, A. Gillenwater, R. Alizadeh-Naderi, A. K. El-Naggar, and R. Richards-Kortum, "Detection and diagnosis of oral neoplasia with an optical coherence microscope," *J. Biomed. Opt.* **9**(6), 1271–1280 (2004).

61. A. Garofalakis, G. Zacharakis, G. Filippidis, E. Sanidas, D. D. Tsiftsis, E. Stathopoulos, M. Kafousi, J. Ripoll, and T. G. Papazoglou, "Optical characterization of thin female breast biopsies based on the reduced scattering coefficient," *Phys. Med. Biol.* **50**(11), 2583–2596 (2005).

62. J. C. Kah, K. Y. Wong, K. G. Neoh, J. H. Song, J. W. Fu, S. Mhaisalkar, M. Olivo, and C. J. Sheppard, "Critical parameters in the pegylation of gold nanoshells for biomedical applications: An *in vitro* macrophage study," *J. Drug Target.* **17**(3), 181–193 (2008)

63. H. J. van Staveren, C. J. M. Moes, J. van Marie, S. A. Prahl and M. J. C. van Gemert, "Light scattering in Intralipid-10% in the wavelength range of 400–1100 nm," *Appl. Opt.* **30**(31), 4507–4514 (1991).